Learning Ego 3D Representation as Ray Tracing

Jiachen Lu[1], Zheyuan Zhou[1], Xiatian Zhu[2], Hang Xu[3], and Li Zhang[1⋆]

[1]Fudan University [2]University of Surrey [3]Huawei Noah's Ark Lab

https://fudan-zvg.github.io/Ego3RT

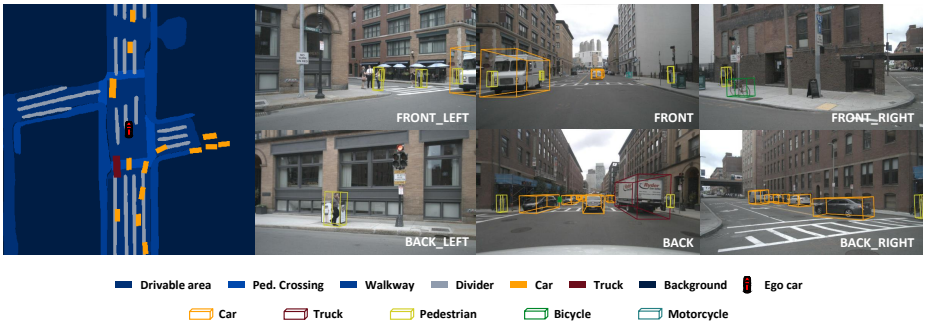

Fig. 1: We propose an ego 3D representation learning method that extracts 3D representation in bird's-eye-view (BEV) from multi-view cameras (*right*). With the aid of our 3D representation, multiple tasks can be executed efficiently in a single model: BEV segmentation (*left*) and 3D object detection (*right*).

Abstract. A self-driving perception model aims to extract 3D semantic representations from multiple cameras collectively into the bird's-eye-view (BEV) coordinate frame of the ego car in order to ground downstream planner. Existing perception methods often rely on error-prone depth estimation of the whole scene or learning sparse virtual 3D representations without the target geometry structure, both of which remain limited in performance and/or capability. In this paper, we present a novel end-to-end architecture for ego 3D representation learning from an arbitrary number of unconstrained camera views. Inspired by the ray tracing principle, we design a polarized grid of "imaginary eyes" as the learnable ego 3D representation and formulate the learning process with the adaptive attention mechanism in conjunction with the 3D-to-2D projection. Critically, this formulation allows extracting rich 3D representation from 2D images without any depth supervision, and with the built-in geometry structure consistent *w.r.t* BEV. Despite its simplicity and versatility, extensive experiments on standard BEV visual tasks (*e.g.*,

⋆ Li Zhang (lizhangfd@fudan.edu.cn) is the corresponding author with School of Data Science, Fudan University.

camera-based 3D object detection and BEV segmentation) show that our model outperforms all state-of-the-art alternatives significantly, with an extra advantage in computational efficiency from multi-task learning.

Keywords: 3D object detection, BEV segmentation, Multi-camera.

1 Introduction

Taking an image as input, existing vision models usually either ignore (*e.g.*, image classification [6, 10, 26]) or consume directly (*e.g.*, object detection [17, 22, 41], image segmentation [3, 13, 38]) the coordinate frame of input during results prediction. Nonetheless, this paradigm does not match the perception circumstance of self-driving out-of-the-box, where the input source is multiple cameras each with a specific coordinate frame, and the perception models for downstream tasks (*e.g.*, 3D object detection, lane segmentation) need to make predictions in the coordinate frame of the ego car, totally *different* from all the input frames. That is, a self-driving perception model needs to reason about 3D semantics from 2D visual representations of multi-view images, which is non-trivial and highly challenging.

In the literature, existing methods mostly take the following two strategies. The ***first*** strategy show in Figure 2(a) (*e.g.*, LSS [20], CaDDN [21]) relies on pixel-level depth estimation, as it can be used to project the 2D visual representation to the ego coordinate frame alongside intrinsic and extrinsic projection. Often, the depth prediction is end-to-end learned within the model without supervision [20], or with extra 3D supervision [21]. A downside of these methods is that depth estimation in unconstrained scenes is typically error-prone, which would be further propagated down to the subsequent components. This is also known as the *error propagation* problem, largely inevitable for such pipelines.

To solve this above issue, the ***second*** strategy (*e.g.*, Image2Map [25], OFT [24], DETR3D [32]) eliminates the depth dimension via directly learning 3D representations from 2D images through architecture innovation. This approach has shown to be superior over depth-estimation based counterparts, implying that learning 3D representation is a superior general strategy. In particular, Image2Map [25] and PON [23] leverage a Transformer or FC layer to learn the projection from 2D image frame to the bird's-eye-view (BEV) coordinate frame forwardly. As is shown in Figure 2(b), However, their 3D representation is structurally inconsistent with 2D counterparts as no rigorous intrinsic and extrinsic projection can be leveraged, *i.e.*, no explicit one-one correspondence relation across the coordinate frames, consequently resulting in sup-optimal solutions. The recent state-of-the-art DETR3D [32] formulates a 3D representation learning model with a Transformer model, inspired by contemporary image based object detection models [2]. However, its 3D representation is not only *sparse*, but *virtual* in the sense of no geometry structure explicitly involved *w.r.t* the ego coordinate frame, and is thus unable to conduct dense prediction tasks such as segmentation.

In this work, we present a novel ego 3D representation learning method that overcomes all the aforementioned limitations in an end-to-end formulation. This is inspired by the ray tracing principle [33] in computer graphics, which simulates the light transport process from the sources to human eyes in graphic rendering. Rather than taking the optical sources as inception, ray tracing *backtracks* the optical paths from the imaginary eyes to the objects in an opposite way. Analogously, we start with introducing a polarized grid of dense "imaginary eyes" for BEV representation, with each eye naturally occupying a specific geometry location with the depth information involved. As is shown in Figure 2(c), for learning 3D representation including height information intrinsically absent in BEV, we initialize each eye using a uniform value and leave the eyes to look backward surrounding 2D visual representations subject to the intrinsic and extrinsic 3D-to-2D projection. With the adaptive attention mechanism, eyes focus dynamically on 2D representations and directly learn to approximate missing height information in a data driven manner. Critically, our architecture can be applied for both sparse (*e.g.*, 3D object detection) and dense (*e.g.*, BEV semantic segmentation) prediction tasks. We term our method *Ego 3D representation learning as Ray Tracing* (***Ego3RT***).

We make the following **contributions**: **(1)** We propose a novel ego 3D representation learning architecture, inspired by the ray tracing perspective. **(2)** Without depth supervision, our method can learn geometrically structured and dense 3D representations from arbitrary camera rigs *w.r.t* the ego car coordinate frame, subject to the intrinsic and extrinsic 3D-to-2D projection. This is achieved by adapting the ray tracing concept, where we first introduce a polarized grid of "imaginary eyes" as the learnable BEV representation, and then trace them *backwards* to camera rigs by formulating the learning process of this 3D representation into an adaptive attention framework. **(3)** Expensive experiments on 3D object detection and lane segmentation self-driving tasks validate the superiority of our method over state-of-the-art alternative methods, often by a large performance gap. In particular, Ego3RT enables multi-task learning by representation sharing between object detection and BEV segmentation whilst still yielding superior performance, hence more computationally efficient and economically scalable for self-driving.

2 Related work

Depth-based strategy Benefited from well-studied depth estimation, Pseudo-lidar [31], Pseudo-lidar++ [37] and AM3D [16] separate the 3D representation learning into monocular depth estimation and 3D detection. CaDDN [21] uses a supervised depth estimation network to accumulate a more precise position of each voxel from the front-view features. These dual-step methods rely on extra depth estimation data and are not end-to-end trainable. LSS [20] and FIERY [11] achieve the front-view features lifting in an end-to-end manner with the depth distribution prediction to generate the intermediate 3D representations. How-

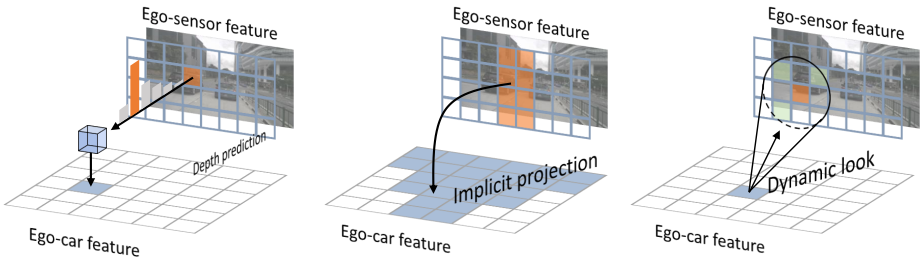

(a) (b) (c)

Fig. 2: Comparison of dense 3D representation learning strategies. (a) The ***first*** strategy, represented by LSS [20], CaDDN [21], is based on dense pixel-level depth estimation. (b) The ***second*** strategy represented by PON [23] bypasses the depth estimation by learning implicit 2D-3D projection. (c) ***Our*** strategy that backtracks 2D information from "imaginary" eyes specially designed in the BEV's geometry.

ever, weakly-constrained depth estimation is error-prone, with the depth error propagated to limit the subsequent 3D localization.

Depth-free strategy OFT [24] simply hypothesizes a uniform distribution over the depth, leading to poor performance in the 3D detection task. Rather than predicting depth, [4, 23, 25, 35] opt to exploit the 3D-to-2D projection process. PYVA [35] shows that the correspondence between 2D features and 3D features can be implicitly learned by cross attention. NEAT [4] further proposes a variation of cross attention for the same purpose. PON [23] and Image2Map [25] resort to a Transformer or FC layer to learn a correspondence between images and 3D features. While decently estimating the 3D-to-2D relationship, a clear limitation is that these models ignore the intrinsic one-one correspondence. Recently, DETR3D [32] learns sparse 3D representations with a Transformer by using sparse queries to detect 3D objects. However, this 3D representation has no geometry structure, making it incapable of performing dense prediction tasks. In this work, we present Ego3RT, a novel end-to-end trainable ego 3D representation learning architecture that solves all the above limitations. Critically, it can learn 3D ego representation from unconstrained camera rigs without any 3D or depth supervision, achieving superior performance on BEV visual tasks even in a more efficient multi-task model design.

3 Method

Our architecture can be divided into two components: (1) ego 3D representation learning (***Ego3RT***) and (2) downstream task head.

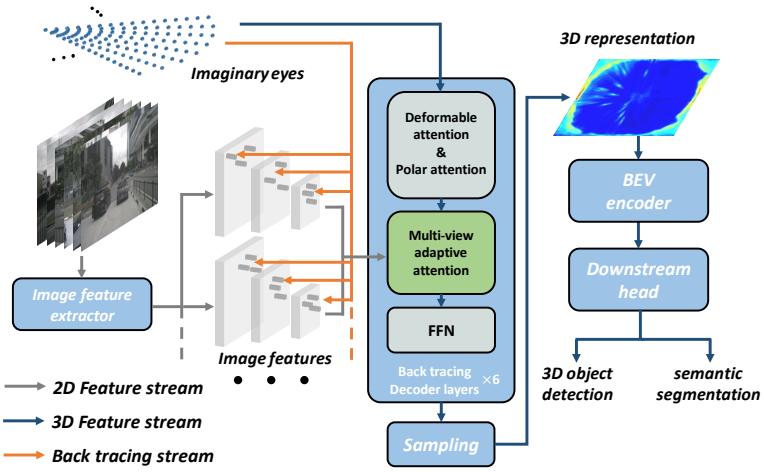

Fig. 3: Our pipeline comprises two stages: learning ego 3D representation from 2D features and executing multiple downstream tasks based on 3D representation. The gray lines represent the 2D feature stream while the blue lines represent the 3D feature stream. Besides, the orange lines specify our back tracing path.

3.1 Ego3RT: Ego 3D representation learning

Ego3RT consists of two parts: image feature extractor and back tracing decoder. In addition, to illustrate back tracing decoder clearly, we will first introduce its components – imaginary eyes, tracing 3D backwards to 2D mechanism and multi-view multi-scale adaptive attention.

Image feature extractor Given a set of images $\mathcal{I} = \{\mathbf{p}_1, \mathbf{p}_2, \cdots \mathbf{p}_{N_{\text{view}}}\}$ from multiple camera sensors (*i.e.*, multiple views), where each image $\mathbf{p}_t \in \mathbb{R}^{H \times W \times 3}$ with t the index of surrounding cameras (*e.g.*, $N_{\text{view}} = 6$ for nuScenes). These images are then encoded by a single shared ego-sensor feature extractor, including a CNN and a transformer encoder. ResNet [10] is used to extract image feature maps at N_{scale} spatial resolutions. To capture global context information, we further apply a transformer encode [41] at each resolution individually. As a result, we obtain the multi-view multi-scale self-attentive 2D representation $\{\mathbf{x}_l^{(t)}\}_{l=1}^{N_{\text{scale}}}$, where $\mathbf{x}_l^{(t)} \in \mathbb{R}^{H_l \times W_l \times C_l}$, $H_l = \frac{H}{4*2^l}, W_l = \frac{W}{4*2^l}$, $t \in [1, \cdots, N_{\text{view}}]$.

Imaginary eyes From this part, we will specify how Ego3RT learning 3D representation from 2D. To avoid exhaustive pixel-level prediction and inconsistent coordinate projection, we draw an analogue in the back tracing idea from ray tracing [33]. We start with introducing a polarized grid of dense "imaginary eyes" shown in Figure 4, for BEV representation, with each eye naturally occupying a specific geometry location with built-in depth information. The grid of eyes are

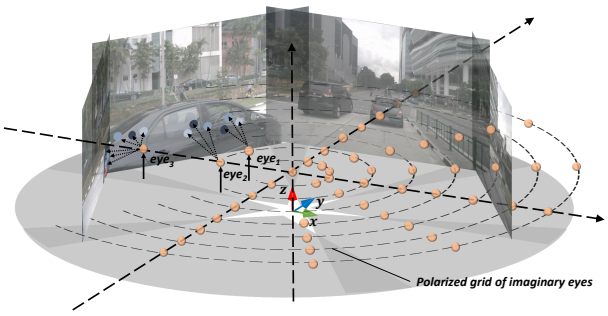

Fig. 4: An illustration of tracing 3D backwards to 2D mechanism for imaginary eyes. The golden balls represents the polarized grid of dense "imaginary eyes". Specially, for eyes have multiple visible images (e.g. eye_3), they backtrack to multiple images, while eyes having only single visible image (e.g. eye_1) backtrack to single image. The blue points on image from light blue to deep show their degree of significance to their eye, thus facilitating the adaptive attention.

in size of $N_{\text{eyes}} = R \times S$, where R is the number of eyes on each polar ray, and S is the number of these polar rays. To construct or, "render" our BEV representation, these imaginary eyes send rays *backwards* to 2D visual representation following the above 3D-2D projection routine (which will be described later). Since each eye only occupies a single, fixed geometry location, tracing back at its corresponding 2D position alone is less informative due to limited local observation. To solve this problem, we propose to encourage the eyes look around to focus adaptively on pivotal feature points across multiple scale per image and multiple camera views. This results in our multi-view multi-scale adaptive attention module (MVAA). And finally, the features of these imaginary eyes will be the final 3D representation.

Tracing 3D backwards to 2D To specify the tracing back mechanism, we first illustrate coordinate transformation between 3D and 2D. In typical cases, we usually have one LIDAR coordinate (3D), N_{view} camera coordinate (3D) and N_{view} image coordinate (2D). A 3D point $\mathbf{x}_{\text{lidar}}$ can be projected to image point $\mathbf{x}_{\text{img}}^{(t)}$ of t^{th} camera by the projection matrix $\mathbf{M}^{(t)} = \mathbf{M}_{\text{in}}^{(t)}\mathbf{M}_{\text{ex}}^{(t)}$. Details of projection matrix will be illustrated in supplement. If the $\mathbf{x}_{\text{img}}$ is inside the image, we say that the image is visible to the corresponding $\mathbf{x}_{\text{lidar}}$. In our method, imaginary eyes are encouraged to "look" around their 2D projection point in each image coordinate. We denote the set of visible images of the q^{th} eyes as $\mathcal{I}_q \subset \mathcal{I}$.

Multi-view multi-scale adaptive attention (MVAA) MVAA is the core of transferring 2D representation into 3D. We formulate the learning of these imaginary eyes in an adaptive self-attention detection framework [41]. This is based on an idea of *regarding the eyes as object queries*, denoted as $\mathbf{y} \in \mathbb{R}^{C \times N_{\text{eye}}}$. Let $\mathbf{r} \in \mathbb{R}^{3 \times N_{\text{eye}}}$ be the location of eyes in ego car coordinate. Formally, each eye

(*i.e.*, query) will dynamically choose N_{point} feature points at every scale of 2D image representation. This gives us a total of $N_{\text{scale}} \times |\mathcal{I}_q| \times N_{\text{point}}$ feature points. Our MVAA then chooses the most significant feature points from them and fuse them across multiple scales and views into the desired 3D representation. The process can be expressed as

$$\begin{aligned}&\text{MVAA}(\mathbf{y}_q, \mathbf{r}_q, \{\{\mathbf{x}_l^{(t)}\}_{l=1}^{N_{\text{scale}}}\}_{t=1}^{N_{\text{view}}}) = \\ &\underset{h\in\{N_h\}}{\text{concat}} \mathbf{W}_h \left[\sum_{l\in\{N_{\text{scale}}\}} \sum_{t\in\mathcal{I}_q} \sum_{k\in\{N_{\text{point}}\}} \mathbf{A}_{hltk} \cdot \mathbf{W}'_h \phi\left(x_l^{(t)}, \mathbf{M}^{(\mathbf{t})}\mathbf{r} + \mathbf{\Delta r}_{hvlk}\right) \right] \end{aligned} \tag{1}$$

Vector $\mathbf{y}_q$ is the q^{th} query (eye), $\mathbf{r}_q$ is its position, N_h is the head number, $\mathbf{M}^{(t)}$ is the projection matrix. $\mathbf{A}$ and $\mathbf{\Delta r}$ are conditioned on $\mathbf{y}_q$ by learnable parameters:

$$\mathbf{A} = \text{softmax}_{tk}(\mathbf{W}_q^{(\mathbf{A})}\mathbf{y}_q) \tag{2}$$

with learnable parameter $\mathbf{W}_q^{(\mathbf{A})} \in \mathbb{R}^{N_h \times N_{\text{scale}} \times |\mathcal{I}_q| \times N_{\text{point}} \times C}$, and

$$\mathbf{\Delta r} = \mathbf{W}_q^{(\mathbf{r})}\mathbf{y}_q + \mathbf{b}_q^{(\mathbf{r})} \tag{3}$$

with learnable parameter $\mathbf{W}_q^{(\mathbf{r})} \in \mathbb{R}^{N_h \times N_{\text{scale}} \times |\mathcal{I}_q| \times N_{\text{point}} \times 2 \times C}$, and fixed parameter $\mathbf{b}_q^{(\mathbf{r})} \in \mathbb{R}^{N_h \times N_{\text{scale}} \times |\mathcal{I}_q| \times N_{\text{point}} \times 2}$. To avoid these N_{point} feature points collapse into one point, $\mathbf{b}_q^{(\mathbf{r})}$ is initialized with $|\mathbf{b}_q^{(\mathbf{r})}[\cdot,\cdot,\cdot,k]| = k$, so that the more N_{point}, the larger offset of these feature points can be achieved. Therefore, N_{point} can be utilized to control the receptive field. $\phi(x, r)$ represents access r^{th} feature points from x by index. For adaptively assigning the significance to $N_{\text{scale}} \times |\mathcal{I}_q| \times N_{\text{point}}$ points, the `Softmax` function is applied across all the attended feature points, scales, and views:

$$\sum_{l\in\{N_{\text{scale}}\}} \sum_{t\in\mathcal{I}_q} \sum_{k\in\{N_{\text{point}}\}} \mathbf{A}_{hltk} = 1 \tag{4}$$

Back tracing decoder Technically, back tracing decoder takes randomly initialized features of imaginary eyes and scales of 2D feature provided by image feature extractor as input, and finally outputs the fine-grained features of imaginary eyes as 3D representation. Back tracing decoder is made up with a stack of attention layers adapted from the transformer decoder layers [17]. As shown in Figure 3, each layer stacks two self-attention modules and one cross-attention module in order: deformable attention module [41], polar attention and MVAA. Compared to self-attention, deformable attention is more memory efficient. On the on 3D representation, we apply a standard self-attention on the eyes of same polar ray for polar attention. Also, the feed-forward network (FFN) block is equipped with a depth-wise convolution like [30]. As illustrated before, MVAA is responsible for back tracing 2D features into 3D representation.

Table 1: Comparison of different paradigms on the nuScenes `val` set. FCOS3D† is trained with 1x learning schedule, depth weight 0.2 and is finetuned on another FCOS3D checkpoint. PGD† is trained with 2x learning schedule, depth weight 0.2 on another PGD checkpoint. DETR3D† and Ego3RT† are initialized from the same pretrained FCOS3D checkpoint. Ego3RT‡ is initialized from the pretrained DD3D checkpoint.

Methods	mATE↓	mASE↓	mAOE↓	mAVE↓	mAAE↓	mAP↑	NDS↑
FCOS3D [29]	0.790	**0.261**	0.499	1.286	**0.167**	0.298	0.377
DETR3D [32]	0.860	0.278	**0.327**	**0.967**	0.235	0.303	0.374
PGD [28]	0.732	0.263	0.423	1.285	0.172	0.336	0.409
Ego3RT(Ours)	**0.714**	0.275	0.421	0.988	0.292	**0.355**	**0.409**
FCOS3D† [29]	0.754	**0.260**	0.486	1.331	**0.158**	0.321	0.395
DETR3D† [32]	0.765	0.267	0.392	0.876	0.211	0.347	0.422
PGD† [28]	0.667	0.264	0.435	1.276	0.177	0.358	0.425
Ego3RT(Ours)†	**0.657**	0.268	**0.391**	**0.850**	0.206	**0.375**	**0.450**
Ego3RT(Ours)‡	**0.582**	0.272	**0.316**	**0.683**	0.202	**0.478**	**0.534**

3.2 Downstream task head design

BEV sampling. Before the features of imaginary eyes being processed at downstream task, we first grid sample the polarized features into the rectangular ego car coordinate system to match with dataset annotation.

BEV encoder. To encode the 3D representation for multiple tasks, we adopt the same BEV encoder module from OFT [24]. This kind of sub-network is also widely used in the LiDAR-based 3D detector [12, 34].

Downstream task head. While the previously mentioned stage has generated a dense BEV features, we adopt the popular 3D detection head from CenterPoint [36] for our detection task. For the BEV segmentation task, we choose a group of progressive up-sampling convolution-based semantic segmentation decoder heads. Details are shown in Supplement.

4 Experiments

4.1 Setup

Dataset. We evaluate the proposed model on the nuScenes [1] dataset, a large-scale autonomous driving dataset with 1000 driving scenes. Specifically, for multi-camera 3d object detection, it provides streams of images of 6 cameras covering all round from these 1000 scenes, which are then split into 700/150/150

Table 2: Comparisons to top-performing works on the nuScenes `test` set. ‡ represents that the method uses external data other than nuScenes 3D box annotations. DD3D‡ uses extra data for depth estimation. DETR3D‡ and Ego3RT‡ are initialized from the pre-trained DD3D checkpoint.

Methods	mATE↓	mASE↓	mAOE↓	mAVE↓	mAAE↓	mAP↑	NDS↑
MonoDIS	0.738	0.263	0.546	1.553	0.134	0.304	0.384
CenterNet [39]	0.658	0.255	0.629	1.629	0.142	0.338	0.400
FCOS3D [29]	0.690	0.249	0.452	1.434	**0.124**	0.358	0.428
PGD [28]	0.626	**0.245**	**0.451**	1.509	0.127	0.386	**0.448**
Ego3RT(Ours)	**0.599**	0.268	0.470	**1.169**	0.172	**0.389**	0.443
DD3D‡ [19]	0.572	**0.249**	**0.368**	1.014	**0.124**	0.418	0.477
DETR3D‡ [32]	0.641	0.255	0.394	**0.845**	0.133	0.412	**0.479**
Ego3RT(Ours)‡	**0.549**	0.264	0.433	1.014	0.145	**0.425**	0.473

scenes respectively for training, validation, and testing. nuScenes also provide informative annotations of the map. We choose 5 segmentation tasks: drivable area, pedestrian crossing, walkway, carpark, and divider.

Metrics. To evaluate performance, mean Average Precision (mAP) [8] and NuScenes Detection Score (NDS) [1] are reported. The segmentation task uses Intersection over Union(IoU) to assess the performance. As done by the LSS [20], we create a binary image for each element based on a specific threshold to evaluate with the ground truth image.

Implementation details. Following FCOS3D [29] and DETR3D [32], ResNet-101 [10], with 3rd and 4th stages equipped with deformable convolutions is applied as our image backbone. The following deformable DETR encoder then utilizes multi-scale feature maps from the 2nd, 3rd, and 4th stages of the backbone. We use eyes of density 80×256 for Ego3RT and be sampled to rectangular 160×160 grids by BEV sampling. For the BEV encoder, we use 8 Bottleneck block [10] identical to OFT [24]. In the segmentation task, we set our ground-truth BEV segmentation map of 480×480 size with 0.2m/pixel resolution. Therefore, 1 block of the upsampling module with the bilinear upsampling ratio of $3\times$ is adopted to mitigate lossing details of the screen. Additionally, loss functions are illustrated in supplement.

Training & testing. Our models are trained 24 epoch with `AdamW` [14] of base learning rate 2.5×10^{-4} and weightdecay 0.01. Especially, the learning rate of the backbone is 1/10 of the global learning rate and the parameter of batch normalizations of backbone still participate in fine-tuning. To avoid over-fitting, we apply an early stop at 16 epoch. Since a total batch size of 48 across six cameras

Table 3: Comparison of BEV semantic segmentation IoU on the nuScenes `val` set. Multi means wether generate a full surrounded BEV segmentation map from multi-view images. "-" represents the unprovided result. Single-task version Ego3RT uses EfficientNet-B0 [27] as the image backbone to align with OFT [24] and LSS [20]. Multi-task version Ego3RT¶ means we only train the segmentation head with the pretrained detection model frozen.

Method	multi?	Drivable	Crossing	Walkway	Carpark	Divider
VED [15]	✗	54.7	12.0	20.7	13.5	-
VPN [18]	✗	58.0	27.3	29.4	12.3	-
PON [23]	✗	60.4	28.0	31.0	18.4	-
OFT [24]	✗	62.4	30.9	34.5	23.5	-
LSF [7]	✗	61.1	33.5	37.8	25.4	-
Image2Map [25]	✗	74.5	**36.6**	35.9	31.3	-
OFT [24]	✓	71.7	-	-	-	18.0
LSS [20]	✓	72.9	-	-	-	20.0
Ego3RT(Ours)	✓	**79.6**	**48.3**	**52.0**	**50.3**	**47.5**
Ego3RT(Ours) ¶	✓	**74.6**	33.0	**42.6**	**44.1**	**36.6**

on eight NVIDIA A6000 GPUs is used, we apply synchronized implementation for every batch normalization. During the training process, we use the input image of 1500×900 resolution with only photometric distortion augmentation. Random flip, random rotation, and random scaling are applied to the 3D feature. Our 3D detection head is trained with class-balanced grouping method [40] (but no DS sampling) as default. After the detection head is well trained, we fix the parameters of Ego3RT and fine-tune our segmentation head for multi-task.

4.2 Comparison with state of the art

3D object detection. We compare our model with previous state-of-the-art methods on both nuScenes validation set and test set. Following FCOS3D [29] and DETR3D [32], all our experiments are trained using ResNet-101 with deformable convolution as backbone for prototype verification. Models without special notification is initialized from a ResNet-101 checkpoint which pre-trained on ImageNet [5]. We also present the result of our model on pre-trained checkpoints from FCOS3D [29] and DD3D [19]. In specific, the DD3D [19] fintunes on extra DDAD15M [9] dataset. **To be noted, the monocular-camera paradigms [28, 29] and the multi-camera ones can be fairly compared.** They all take 6 cameras as input, but the monocular paradigms process these input images independently while the multi-view paradigms process these input images simultaneously.

Table 1 summarizes our multi-camera 3D object detection results on the nuScenes `validation` set. The upward arrow means the large the better while the downward one means the small the better. Our method leads in both `mAP`

Table 4: Comparisons of detection performance in non-overlap region and overlap region. FCOS3D is trained with 1x learning schedule, depth weight 0.2 and is finetuned on another FCOS3D checkpoint. PGD is trained with 2x learning schedule, depth weight 0.2 and is finetuned on another PGD checkpoint. DETR3D and Ego3RTare initialized from a same pretrained FCOS3D checkpoint.

Methods	overlap?	mATE↓	mASE↓	mAOE↓	mAVE↓	mAAE↓	mAP↑	NDS↑
FCOS3D [29]	✗	0.747	**0.260**	0.487	1.351	**0.156**	0.320	0.395
PGD [28]	✗	0.658	0.263	0.425	1.290	0.178	0.357	0.426
DETR3D [32]	✗	0.769	0.267	**0.390**	0.893	0.215	0.343	0.419
Ego3RT(Ours)	✗	**0.655**	0.267	0.395	**0.854**	0.208	**0.371**	**0.448**
FCOS3D [29]	✓	0.816	0.272	0.571	1.084	**0.173**	0.229	0.329
PGD [28]	✓	0.768	0.274	0.495	1.090	0.186	0.255	0.354
DETR3D [32]	✓	0.807	0.273	0.453	**0.788**	0.184	0.268	0.384
Ego3RT(Ours)	✓	**0.671**	**0.268**	**0.347**	0.797	0.212	**0.298**	**0.420**

and `NDS`. Specially, it achieves the best in **transition error** (`mATE`), proving back tracing strategy's ability in localization reasoning. Just with simple attention, Ego3RT outperforms localization prediction than the well-designed PGD.

Table 5: Ablation on the effectiveness of adaptive attention mechanism.

adaptive?	mATE↓	mASE↓	mAOE↓	mAVE↓	mAAE↓	mAP↑	NDS↑
✗	0.688	0.272	0.403	**0.835**	0.217	0.365	0.441
✓	**0.657**	**0.268**	**0.391**	0.850	**0.206**	**0.375**	**0.450**

Table 2 shows our results on the nuScenes `test` set. The training sets are the same as the validation set. The least **transition error** (`mATE`) also reflects the overwhelming localization power of back tracing mechanism. We achieve the best `mAP` but the `NDS` is hindered by the attribute error. We have to say that the 2D representation has a manifest advantage on classification over 3D representation.

BEV segmentation. Table 3 summarizes our BEV segmentation results on nuScenes `validation` set. We achieve the best performance in all tasks except the pedestrian crossing, but its overwhelming advantage in other tasks still proves its success. We also present single-task version using ImageNet pretrained Efficient-B0 [27] as our image backbone to make a fair comparison with OFT [24] and LSS [20]. In terms of the single-task version, Ego3RT leads the board with huge superiority.

Table 6: Ablations on polarized grid of imaginary eyes.

polarized grid?	polar attention?	mATE↓	mASE↓	mAOE↓	mAVE↓	mAAE↓	mAP↑	NDS↑
✗	✗	0.673	0.271	0.397	0.901	0.211	0.365	0.437
✓	✗	**0.656**	0.271	0.397	0.881	**0.206**	0.362	0.440
✓	✓	0.657	**0.268**	**0.391**	**0.850**	**0.206**	**0.375**	**0.450**

Table 7: (a) Results with different density of imaginary eyes. (b) Results with different height above the ground of imaginary eyes in meter.

#eyes	96×256	64×256	80×224	80×256
mAP ↑	0.372	0.366	0.372	**0.375**
NDS ↑	0.447	0.444	0.445	**0.450**

height	0m	0.4m	0.8m
mAP ↑	0.375	0.375	0.375
NDS ↑	0.445	0.437	**0.450**

4.3 Qualitative results

We present our visualization in Figure 5. The structural similarity to the ground-truth highlights the superiority of our Ego3RT, which simultaneously generates dynamic object detection and static semantic segmentation results from the 3D representation. In specific, we project all bounding boxes of class *vehicle* in nuScenes from the detection head onto the generated BEV segmentation map for a clear comparison. As can be seen from the perspective of images, our detection results demonstrate appealing localization ability even in distance situations. More qualitative results are shown in supplement.

4.4 Ablation studies

In this section, we will figure out how the performance is established and prove the effectiveness of our innovation. Additional studies are shown in the supplement.

Back tracing mechanism Here, we prove that the back tracing mechanism posses superiority in localization. To eliminate interference of multi-view mechanism, in the top part of Table 4, hence, we validate the 3D detection result only at the non-overlap region where only a monocular camera is used. We show advantage in overall `mAP`, `NDS` metrics at monocular region. Specially, the lowest transition error `mATE` proves the best localization reasoning of Ego3RT .

Multi-view mechanism We will prove the superiority of the multi-view mechanism over the former monocular ones. In the bottom part of Table 4, we validate the 3D detection result at region where only multiple cameras are used. We

Table 8: Comparison of the efficiency and the performance of different configurations of Ego3RT and the other methods. "FPS" is a metric for efficiency standing for frames per second. "Resolution" represents input image shape. "FFN" represents the channel expansion dimension of FFN in Back tracing decoder. "Blocks" notes the number of blocks in BEV encoder. "$\star$" means we test the speed at 1600×900.

Methods	Resolution	Eyes density	FFN	#Blocks	FPS↑	mAP↑	NDS↑
FCOS3D [29]	1600×900	-	-	-	2.0	0.321	0.395
PGD [28]	1600×900	-	-	-	1.5	0.358	0.425
DETR3D [32]	1600×900	-	-	-	**3.0**	0.347	0.422
Ego3RT(Ours)	$1600 \times 900^{\star}$	80×256	1024	8	1.7	**0.375**	**0.450**
Ego3RT(Ours)	1280×768	72×192	1024	8	2.3	0.372	0.438
Ego3RT(Ours)	1280×768	64×128	256	2	**3.0**	0.355	0.423

find that multi-view methods DETR3D and our Ego3RT outperform mono-view methods FCOS3D [29] and PGD [28] remarkably in all metrics. Additionally, Ego3RT achieves overwhelming performance over the other methods in both `mAP` and `NDS`.

Adaptive attention mechanism We state in the method section that the adaptive attention mechanism can approximate missing height information. All the other conditions remaining the same, we switch off the adaptive attention module by fixing learnable parameter $\mathbf{W}_q^{(\mathbf{r})}\mathbf{y}_q$ in Eq. (3) to prove its effectiveness. The results shown in Table 5 prove our statement.

Polarized grid of imaginary eyes We apply a polarized grid of "imaginary eyes" rather than a rectangular grid. Here, we compare these two settings in Table 6. The first line and the second line compare the grid type of eyes without polar attention. Although the polarized grid doesn't show manifest superiority over the rectangular grid, the polarized grid achieves a remarkable advantage in localization prediction (`mATE`). Finally, with the help of polar attention on the eyes of each polar ray, the model achieves the best.

Imaginary eyes Table 7 studies density and height of imaginary eyes. Lower density will lead to coarser feature maps while the higher density imposes a burden on optimization, so a balance should be achieved. Table 7(a) shows that our final choice 80×256 is the optimal choice. Table 7(b) shows that no significant difference exists among the different choices of height.

Efficiency of Ego3RT In Table 8, our Ego3RT (of main configuration) achieves the best mAP and 3rd FPS, and Ego3RT with smaller input image size and imaginary eyes density barely looses its performance while achieves a better efficiency.

Fig. 5: Qualitative results on nuScenes dataset. *Left* is the BEV segmentation map with projected *vehicle* 3D bounding boxes result from detection head. *Right* are in image perspective with prediction results. Different colors stand for different categories.

When Ego3RT further reduces its eyes density, FFN channel expansion dimension and BEV encoder blocks, it reaches the best trade-off between accuracy and efficiency.

5 Conclusion

In this work, we have presented Ego3RT, a novel end-to-end architecture for ego 3D representation learning given multiple unconstrained camera views. In the absence of depth or 3D supervision, it can learn rich and semantic 3D representation with multi-view images efficiently in the ego car coordinate frame. This is realized by drawing an analog from the ray tracing concept, where we create a polarized grid of learnable "imaginary eyes" as the ego 3D representation and formulate the learning with the adaptive attention mechanism subject to the 3D-to-2D projection. It is easy to implement and able to support multiple different tasks. Extensive experiments validate the superiority of our Ego3RT in comparison to state-of-the-art alternatives in terms of both accuracy and versatility.

Acknowledgments

This work was supported in part by National Natural Science Foundation of China (Grant No. 6210020439), Lingang Laboratory (Grant No. LG-QS-202202-07), Natural Science Foundation of Shanghai (Grant No. 22ZR1407500).

References

1. Caesar, H., Bankiti, V., Lang, A.H., Vora, S., Liong, V.E., Xu, Q., Krishnan, A., Pan, Y., Baldan, G., Beijbom, O.: nuscenes: A multimodal dataset for autonomous driving. In: CVPR (2020) 8, 9
2. Carion, N., Massa, F., Synnaeve, G., Usunier, N., Kirillov, A., Zagoruyko, S.: End-to-end object detection with transformers. In: ECCV (2020) 2
3. Chen, L.C., Papandreou, G., Schroff, F., Adam, H.: Rethinking atrous convolution for semantic image segmentation. arXiv preprint (2017) 2
4. Chitta, K., Prakash, A., Geiger, A.: Neat: Neural attention fields for end-to-end autonomous driving. In: ICCV (2021) 4
5. Deng, J., Dong, W., Socher, R., Li, L.J., Li, K., Fei-Fei, L.: Imagenet: A large-scale hierarchical image database. In: CVPR (2009) 10
6. Dosovitskiy, A., Beyer, L., Kolesnikov, A., Weissenborn, D., Zhai, X., Unterthiner, T., Dehghani, M., Minderer, M., Heigold, G., Gelly, S., et al.: An image is worth 16x16 words: Transformers for image recognition at scale. In: ICLR (2021) 2
7. Dwivedi, I., Malla, S., Chen, Y.T., Dariush, B.: Bird's eye view segmentation using lifted 2d semantic features. In: BMVC (2021) 10
8. Everingham, M., Van Gool, L., Williams, C.K., Winn, J., Zisserman, A.: The pascal visual object classes (voc) challenge. IJCV (2010) 9
9. Guizilini, V., Ambrus, R., Pillai, S., Raventos, A., Gaidon, A.: 3d packing for self-supervised monocular depth estimation. In: CVPR (2020) 10
10. He, K., Zhang, X., Ren, S., Sun, J.: Deep residual learning for image recognition. In: CVPR (2016) 2, 5, 9
11. Hu, A., Murez, Z., Mohan, N., Dudas, S., Hawke, J., Badrinarayanan, V., Cipolla, R., Kendall, A.: Fiery: Future instance prediction in bird's-eye view from surround monocular cameras. In: CVPR (2021) 3
12. Lang, A.H., Vora, S., Caesar, H., Zhou, L., Yang, J., Beijbom, O.: Pointpillars: Fast encoders for object detection from point clouds. In: CVPR (2019) 8
13. Long, J., Shelhamer, E., Darrell, T.: Fully convolutional networks for semantic segmentation. In: CVPR (2015) 2
14. Loshchilov, I., Hutter, F.: Decoupled weight decay regularization. In: ICLR (2019) 9
15. Lu, C., van de Molengraft, M.J.G., Dubbelman, G.: Monocular Semantic Occupancy Grid Mapping With Convolutional Variational Encoder-Decoder Networks. IEEE Robotics and Automation Letters (2019) 10
16. Ma, X., Wang, Z., Li, H., Zhang, P., Ouyang, W., Fan, X.: Accurate monocular 3d object detection via color-embedded 3d reconstruction for autonomous driving. In: ICCV (2019) 3
17. Misra, I., Girdhar, R., Joulin, A.: An end-to-end transformer model for 3d object detection. In: ICCV (2021) 2, 7
18. Pan, B., Sun, J., Leung, H.Y.T., Andonian, A., Zhou, B.: Cross-view semantic segmentation for sensing surroundings. IEEE Robotics and Automation Letters (2020) 10
19. Park, D., Ambrus, R., Guizilini, V., Li, J., Gaidon, A.: Is pseudo-lidar needed for monocular 3d object detection? In: ICCV (2021) 9, 10
20. Philion, J., Fidler, S.: Lift, splat, shoot: Encoding images from arbitrary camera rigs by implicitly unprojecting to 3d. In: ECCV (2020) 2, 3, 4, 9, 10, 12
21. Reading, C., Harakeh, A., Chae, J., Waslander, S.L.: Categorical depth distribution network for monocular 3d object detection. In: CVPR (2021) 2, 3, 4

22. Ren, S., He, K., Girshick, R., Sun, J.: Faster r-cnn: Towards real-time object detection with region proposal networks. In: NeurIPS (2015) 2
23. Roddick, T., Cipolla, R.: Predicting semantic map representations from images using pyramid occupancy networks. In: CVPR (2020) 2, 4, 10
24. Roddick, T., Kendall, A., Cipolla, R.: Orthographic feature transform for monocular 3d object detection. In: BMVC (2019) 2, 4, 8, 9, 10, 12
25. Saha, A., Maldonado, O.M., Russell, C., Bowden, R.: Translating images into maps. arXiv preprint (2021) 2, 4, 10
26. Simonyan, K., Zisserman, A.: Very deep convolutional networks for large-scale image recognition. ICLR (2015) 2
27. Tan, M., Le, Q.: Efficientnet: Rethinking model scaling for convolutional neural networks. In: ICML (2019) 10, 11
28. Wang, T., Xinge, Z., Pang, J., Lin, D.: Probabilistic and geometric depth: Detecting objects in perspective. In: Conference on Robot Learning (2022) 8, 9, 10, 11, 13
29. Wang, T., Zhu, X., Pang, J., Lin, D.: Fcos3d: Fully convolutional one-stage monocular 3d object detection. In: CVPR (2021) 8, 9, 10, 11, 13
30. Wang, W., Xie, E., Li, X., Fan, D.P., Song, K., Liang, D., Lu, T., Luo, P., Shao, L.: Pvt v2: Improved baselines with pyramid vision transformer. Computational Visual Media pp. 415–424 (2022) 7
31. Wang, Y., Chao, W.L., Garg, D., Hariharan, B., Campbell, M., Weinberger, K.Q.: Pseudo-lidar from visual depth estimation: Bridging the gap in 3d object detection for autonomous driving. In: CVPR (2019) 3
32. Wang, Y., Guizilini, V.C., Zhang, T., Wang, Y., Zhao, H., Solomon, J.: Detr3d: 3d object detection from multi-view images via 3d-to-2d queries. In: Conference on Robot Learning (2022) 2, 4, 8, 9, 10, 11, 13
33. Whitted, T.: An improved illumination model for shaded display. In: ACM Siggraph 2005 Courses (2005) 3, 5
34. Yan, Y., Mao, Y., Li, B.: Second: Sparsely embedded convolutional detection. Sensors (2018) 8
35. Yang, W., Li, Q., Liu, W., Yu, Y., Ma, Y., He, S., Pan, J.: Projecting your view attentively: Monocular road scene layout estimation via cross-view transformation. In: CVPR (2021) 4
36. Yin, T., Zhou, X., Krahenbuhl, P.: Center-based 3d object detection and tracking. In: CVPR (2021) 8
37. You, Y., Wang, Y., Chao, W.L., Garg, D., Pleiss, G., Hariharan, B., Campbell, M., Weinberger, K.Q.: Pseudo-lidar++: Accurate depth for 3d object detection in autonomous driving. In: ICLR (2019) 3
38. Zheng, S., Lu, J., Zhao, H., Zhu, X., Luo, Z., Wang, Y., Fu, Y., Feng, J., Xiang, T., Torr, P.H., et al.: Rethinking semantic segmentation from a sequence-to-sequence perspective with transformers. In: CVPR (2021) 2
39. Zhou, X., Wang, D., Krähenbühl, P.: Objects as points. arXiv preprint (2019) 9
40. Zhu, B., Jiang, Z., Zhou, X., Li, Z., Yu, G.: Class-balanced grouping and sampling for point cloud 3d object detection. arXiv preprint (2019) 10
41. Zhu, X., Su, W., Lu, L., Li, B., Wang, X., Dai, J.: Deformable detr: Deformable transformers for end-to-end object detection. In: ICLR (2021) 2, 5, 6, 7